

# Simultaneous Artefact-Lesion Extraction for Skin Cancer Diagnosis<sup>\*</sup>

Michael Osadebey<sup>1</sup>, Marius Pedersen<sup>1</sup>, and Dag Waaler<sup>2</sup>

<sup>1</sup> Department of Computer Science, Norwegian University of Science and Technology, Teknologivegen 22, Gjøvik, 2815, Norway [michael.osadebey@ntnu.no](mailto:michael.osadebey@ntnu.no), [marius.pedersen@ntnu.no](mailto:marius.pedersen@ntnu.no)

<sup>2</sup> Department of Health Sciences Science, Norwegian University of Science and Technology, Teknologivegen 22, Gjøvik, 2815, Norway [dag.waaler@ntnu.no](mailto:dag.waaler@ntnu.no)

**Abstract.** In this paper, we propose a method for simultaneous removal of artefact and detection of lesion borders in dermatoscopy images. Our methodology include investigating the influence of colour spaces and popular threshold-based binarization techniques on segmentation accuracy. Based on the investigation, we determine the colour space and binarization techniques that are most suitable for the proposed method. Furthermore, we analyze the relationship between different attributes of 600 dermatoscopy images and the segmentation accuracy of the proposed method. The analysis provide insight on the computation of threshold correction factor that will optimize segmentation accuracy. Performance evaluation results show potential for clinical applications.

**Keywords:** Skin Lesion · Colour Spaces · Set Theory.

## 1 Introduction

Computer aided diagnostic (CAD) systems facilitate image interpretation which assist dermatologists in the early detection and diagnosis of skin cancer to avoid unnecessarily expensive biopsy [1], [2]. Improved diagnostic accuracy of skin cancer and the physicians' level of confidence in clinical diagnosis have been attributed to the use of dermatoscopy images in CAD systems [3], [4].

There are five successive stages of a CAD system for the classification of pigmented skin lesion [5], [6]. It begins with image acquisition using a dermatoscope. The second stage is the extraction of lesion boundary. At the third stage, features are extracted from the segmented lesion, followed by the fourth stage where the number of extracted features are pruned down to only the most relevant features. At the last stage, the selected features are used to classify the lesion as either benign tumor or malignant melanoma.

Segmentation is a very critical stage in a CAD system because the subsequent stages of the workflow leading to reliable and efficient diagnosis is strongly dependent on accurate lesion border detection. Unfortunately, confounding factors

---

<sup>\*</sup> Supported by European Research Consortium and Informatics (ERCIM).

such as poor image quality and the presence of artifacts may pose serious challenge to segmentation task. [7]. Common artifacts in dermatoscopy images are skin hairs which occlude the lesion boundary and clutter the background. Other artefact include clutters such as ruler markings, colour charts, gel bubbles, date stamps and ink markers. Cluttering and occluding objects present high gradients which mimic skin lesion boundaries. Consequently, it becomes challenging for intensity-based image analysis systems to accurately detect the lesion boundary and extract texture information required for classification [8]. To address these challenges, a pre-processing algorithm such as [9], [10], [11], [12] or a robust segmentation algorithm such as [13], [14], [15], [16], [17], which considers each of these confounding factors, is incorporated into a CAD system for the diagnosis of skin cancer [18]. Preprocessing algorithms designed to address these challenges increase resources, computational cost and introduce extraneous features, thereby reducing the efficacy of a CAD system for skin cancer detection.

The introduction of robust segmentation techniques have eliminated the need for pre-processing steps such as shading attenuation, colour illumination correction and contrast enhancement. Nevertheless, there is room for new segmentation techniques to improve the efficiency and reliability of a CAD system. Most current robust segmentation techniques still require hair removal pre-processing step because they perform poorly in the presence of cluttering and occluding objects [19], [20]. Images with hair occlusion is one of the factors which limit the detection accuracy of deep learning techniques in the diagnosis of skin cancer [21]. Pre-processing algorithms for hair elimination and restoration are based on morphological operation and diffusion-based techniques which have the tendency to introduce blurring into the image. Texture restoration within lesion region is an invasive and delicate operation with high risk of distorting the original texture which drastically reduce the quality of the segmented image. When the texture is disturbed it will be difficult to utilize the segmented image for automatic lesion change detection and for inclusion in an efficient and effective CAD tool for skin cancer diagnosis [22].

### Our Contribution

Inspired by [23] on plant leaves segmentation in cluttered and occluded images, this paper will propose a method that can remove artefact and segment lesion in dermatoscopy images without the need for a separate pre-processing step for artefact removal. The algorithm for the proposed method begins with transforming the test image to a suitable colour space. The next step is threshold-based binarization. Finally, we iterate the symmetric difference between the binarized image and its rotated version. This final step simultaneously detect lesion borders and eliminate occlusions and clutters. Two key contributions of this paper on skin analysis from dermatoscopy images are:

**Contribution 1.** Investigate the influence of colour space channels and threshold-based binarization techniques on segmentation accuracy. Based on the investigation, we determine colour channel and binarization techniques for optimizing segmentation accuracy.

**Contribution 2.** Statistically analyze the relationship between image attributes and segmentation accuracy. Based on the analysis, we propose a threshold correction factor to enhance the performance of specific threshold-based segmentation techniques.

## 2 Materials and Methods

### 2.1 Sources of Data

The experiments for this study utilize 600 dermatoscopy images from two databases. Four hundred and sixty four images are from the International Skin Imaging Collaboration (ISIC) archive <https://isic-archive.com/>. The remaining 136 images are from the Dermatology Service of Hospital Pedro Hispano, Matosinhos, Portugal <http://www.fc.up.pt/addi/>. Images from the two databases are single-lesion images acquired with different dimensions. The range of row  $M$  dimensions are  $\{765 \leq M \leq 6668\}$ . Corresponding column  $N$  dimensions are  $\{572 \leq N \leq 4439\}$ . Each image has ground truth provided by certified dermatologists.

### 2.2 Dataset Attributes

In order to evaluate the performance of the proposed method on images with different types of artefact, we classify the database images into five categories. The categories and number of images in each category are normal (233), dark corners (84), hair occlusion (93), clutter (57) and multiple artifacts (133). For each image in a given category, six visual attributes were identified and quantitatively evaluated. Visual attributes are labels that can be given to an image to describe its appearance [24]. The first visual attribute is perceptual quality  $D_1$ . It was evaluated using BRISQUE, a no-reference image quality assessment method proposed by [25]. Metrics for quantifying the remaining visual attributes are defined in Eq. 1 - 4. Second attribute (see Eq. 1) is area of lesion  $D_2$ , where  $A_g$  is the number of pixels within lesion region in the ground truth image. Third attribute (see Eq. 2) is the lesion position  $D_3$  relative to the image centroid, where  $(x_s, y_s)$  and  $(X_g, Y_g)$  are the pixel location of the lesion and image centroids, respectively. Fourth attribute (see Eq. 3) is the eccentricity of lesion  $D_4$ , where  $a, b$  are the semi-major and semi-minor axes lengths of the lesion. The fifth attribute (see Eq. 4) is the level of cluttering and occlusion  $D_5$ , where  $A_{gs}$  is the total number of pixels that do not belong to either lesion nor healthy skin in the test image.

$$D_2 = 100 \left( \frac{A_g}{MN} \right) \quad (1)$$

$$D_3 = \left( \frac{\sqrt{(x_s - X_g)^2 + (y_s - Y_g)^2}}{\sqrt{X_g^2 + Y_g^2}} \right) \quad (2)$$

$$D_4 = \left( \sqrt{1 - \frac{b^2}{a^2}} \right) \quad (3)$$

$$D_5 = 100 \left( \frac{A_{gs}}{MN} \right) \quad (4)$$

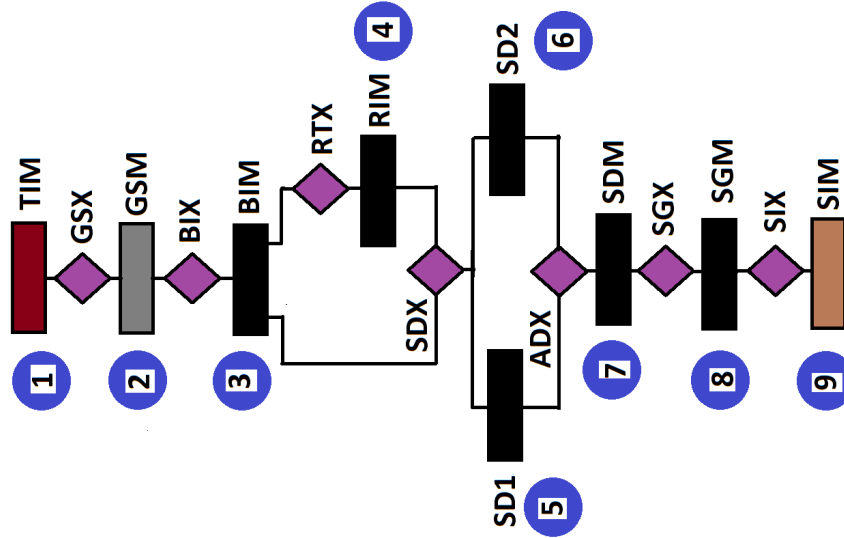


**Fig. 1.** Flow chart for implementation of the proposed skin lesion segmentation in a dermatoscopy image.

### 2.3 Methodology

The flow chart in Fig. 1 and the images in Fig. 2 explains the nine successive steps to implement the proposed method using an hair-occluded test image **TIM** with identification number ISIC\_0000138 from the ISIC challenge 2018.

#### 1. Read Original Image

The RGB test image **TIM** shown in Fig. 2a is read by the algorithm.

#### 2. Colour Space Transformation

The **TIM** is transformed **GSX** to the HSV colour space, followed by the extraction of the saturation channel image **GSM** shown in Fig. 2b.

#### 3. Threshold-based Binarization

The operation of the algorithm requires that the core of the lesion and the lesion borders as well as the cluttering and occluding objects in the binary image are dominated by dark pixels. The reasoning behind this requirement will be obvious in the subsequent steps. To satisfy this requirement, we compute the complement of the **GSM** image. Thereafter, we apply the minimum error method of

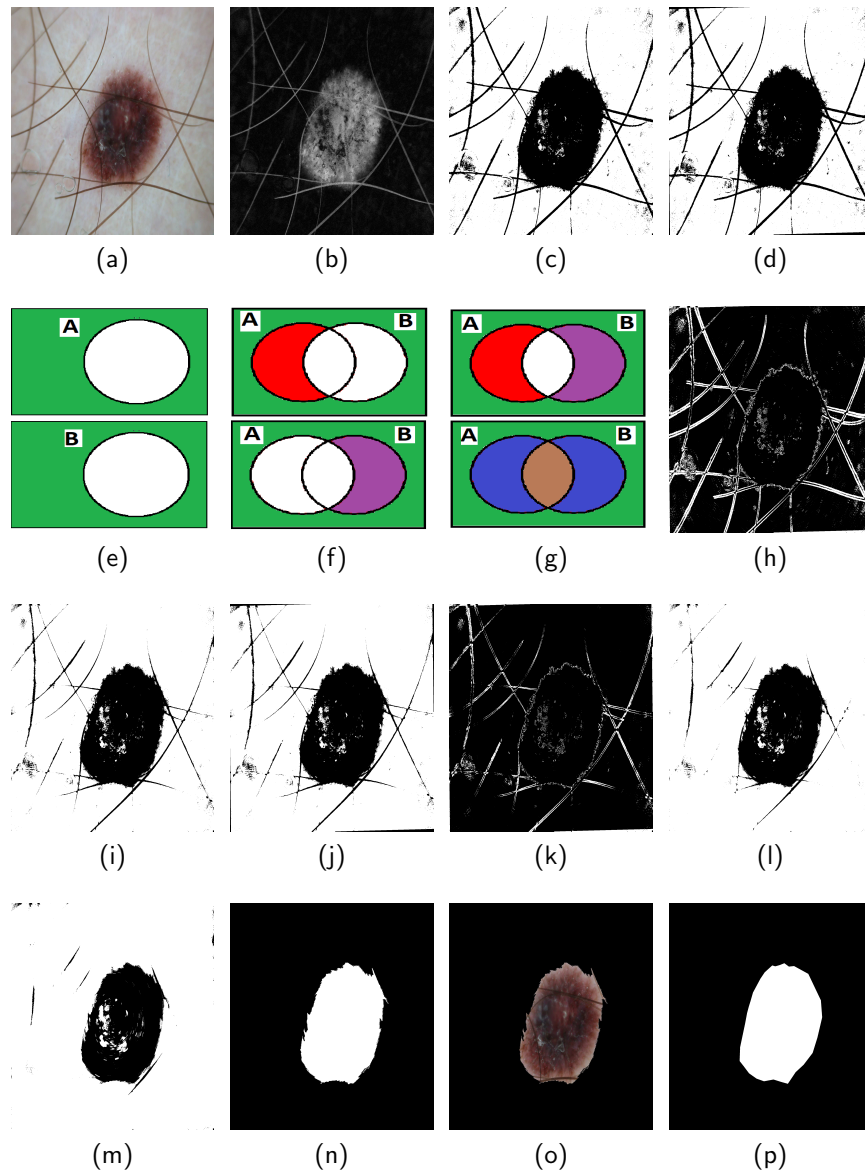


**Fig. 2.** The implementation of proposed method. Detailed explanation is in Section 2.3

thresholding [26] to convert **BIX** the complement image to a binary image shown in Fig. 2c. The computation of the image complement is not required, for example, binary images generated from grayscale and the luminance channel of the CIELAB colour space because they satisfy the operation requirement of the algorithm.

#### 4. Rotation Transformation

We make a copy of **BIM** and rotate **RTX** the duplicate image about its center by a very small angle  $\theta = 1$ . The rotated image **RTM** is shown in Fig. 2d. The stationary binary image and its rotated version are regarded as two separate sets  $A \subset U, B \subset U$ , respectively of logical pixels belonging to a universal set  $U$  (see Fig. 2e).

#### 5. First Set Difference

Prior to displacement, both images are pixel-wise identical. After displacement, both images are no longer pixel-wise identical. We compute **SDX** the set difference **SD1** between the stationary and rotated image:

$$(A \setminus B) = \{x | x \in A \wedge x \notin B\} \quad (5)$$

The set difference **SD1** are pixels in a specific location in the stationary image (red coloured region in Fig. 2f) but are not in the same corresponding pixel location in the displaced image.

#### 6. Second Set Difference

In this step we compute **SDX** the set difference **SD2** between the rotated and the stationary image:

$$(B \setminus A) = \{x | x \in B \wedge x \notin A\} \quad (6)$$

The set difference is the purple coloured region in Fig. 2f.

#### 7. Symmetric Difference

Figure 3g (top figure) shows that the union of  $A$  and  $B$  is the equivalent of three disjoint sets:

$$(A \cup B) = (A \setminus B) \cup (B \setminus A) \cup (A \cap B) \quad (7)$$

Equation 7 above can be expressed as:

$$(A \cup B) = (A \oplus B) \cup (A \cap B) \quad (8)$$

where the first term,  $A \oplus B$  is the symmetric difference of  $A$  and  $B$  (blue coloured region in Fig. 2g). The symmetric difference image **SDM** shown in Fig. 2h is the set of elements which are in either of the sets and not in their intersection. The bright pixels in the symmetric difference image (in Fig. 2h) provides information on all the pixels that are disturbed and weakened by the small angular displacement. The disturbed (shifted) pixels are the boundary pixels of the lesion region. The weakened pixels are the cluttering and occluding objects such as the skin hairs which are severely weakened because their spatial extent and circularity are very low in comparison to lesions. The second term  $(A \cap B)$  on the RHS of Eq. 8 (brown coloured region in Fig. 2g) account for pixels which are preserved under rotation transformation. The preserved pixels shown in Fig. 2h are the dark pixels that dominate the healthy skin and the core of the skin lesion regions.

#### 8. Segmentation mask

Now we will show why the algorithm requires a binary image which the lesion and occluding objects are dominated by dark pixels. The bright pixels in the **SDM**

image shown Fig. 2h (occluding hair and skin lesion borders) are used to replace (erase) corresponding locations (dark pixels) in the stationary image shown in Fig. 2c. This pixel replacement action simultaneously reduces hair occlusion and detect the lesion border producing the image shown in Fig. 2i. Borrowing knowledge from [15], a single operation of computing the symmetric difference image may not be sufficient to detect all the hairs and skin lesion boundary pixels. For this reason, the computation of the **SDM** is iterated  $\beta$  number of times:

$$\beta = \lfloor \log_2(sE) \rfloor \quad (9) \quad sE = 100 \left( \frac{A_s}{MN} \right) \quad (10) \text{ where } sE$$

is a new dataset attribute which we refer to as the spatial extent and  $A_s$  is the total number of pixels that describe the region occupied by the lesion, cluttering and occluding objects in a test image. The attribute  $sE$  is logarithmically transformed to scale down its relatively large range of values. In the second iteration, the output from the first iteration (Fig. 2i) is rotated  $\phi = 1$  about the image centroid to produce the image shown in Fig. 2j. Figure 3k is the **SDM** between Fig. 2i and Fig. 2j. Figure 3l is the output of the second iteration obtained by using the bright pixels in Fig. 2k to replace the dark pixels in Fig. 2i. Figure 3m is the binary image obtained after 5 iterations. The segmentation mask shown in Fig. 2n was derived after area thresholding to remove small structures and hole filling operation.

#### 9. Segmented RGB Image

The segmented image **SIM** shown in fig. 2o is a RGB image. The three colour channels are derived **SIX** by pixel-wise multiplication of each colour channel of the original dermatoscopy image with the segmentation mask followed by vector summation of the three channels. The ground truth image is shown in Fig. 2p

### 3 Experiments and Results

This study has three sessions of experiments. The first session is performance evaluation. In the second session, we analyze the performance evaluation results. Based on the analysis, we determine the binarization techniques that requires correction factor. The third session applies threshold correction factor to relevant binarization techniques.

#### 3.1 Performance Evaluation

The proposed method was evaluated on the 600 test images using thirteen colour channels from four colour spaces. The colour channels are denoted RGB (r,g,b,G), where G denote the gray scale, HSV (h,s,v), CIELAB (L,A,B) and CIEXYZ (x,y,z). The preliminary segmentation for each colour space experiment was implemented using five different threshold-based techniques. Notations for the threshold techniques are ISODATA [27], MEAN [28], MINERROR [26], MOMENT [29] and OTSU [30]. We adopt Dice similarity index as the evaluation metric because it has been consistently used since the inception of the ISIC

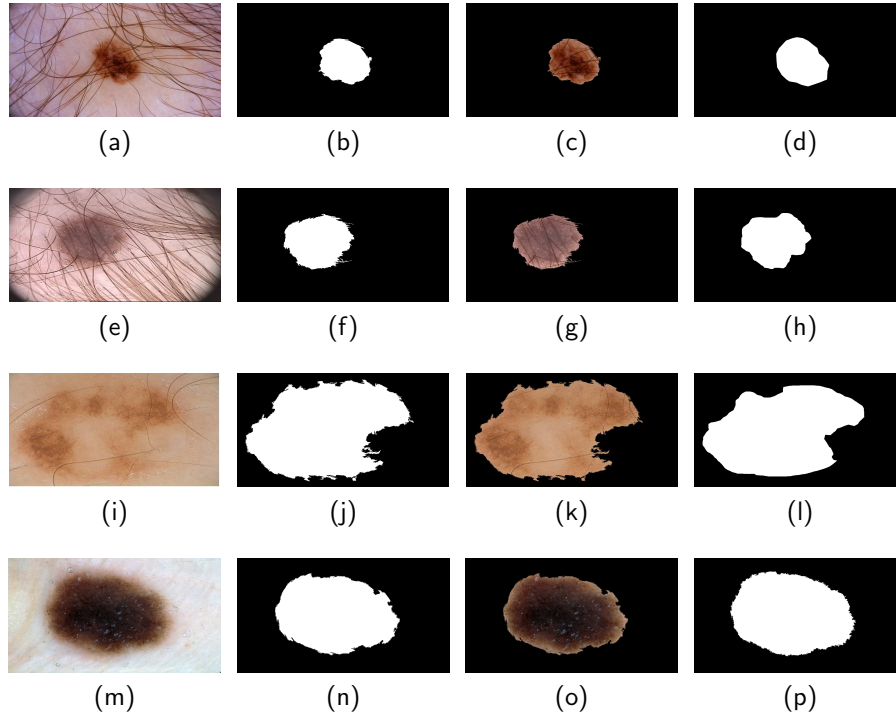


**Fig. 3.** Segmentation results before the application of correction factor to the binarization techniques. The first, second, third and fourth columns are the test image, segmented mask, segmented RGB image and the ground truth image, respectively

challenge. Table 1 display the mean and standard deviation (in bracket) Dice scores. Letter F in the table indicates Dice score less than 0.65. The results from Table 1 suggests that not all colour spaces are suitable for segmentation. Also, segmentation accuracy varies with the choice of colour space and binarization technique. Furthermore, the saturation channel of the HSV colour space can be considered the optimal colour channel for skin lesion segmentation.

Examples of segmentation results for the saturation channel of the HSV colour space are displayed in Fig. 4. The first, second, third and last column of Fig. 4 are the test image, segmented mask, segmented RGB image and ground truth image, respectively. First row of Fig. 4 are the results for hair-occluded test image, ISIC\_0000095 using MINERROR thresholding technique with parameters ( $\beta = 5, \phi = 1$ ). Second row show the result for another hair-occluded test image IMD003 using OTSU technique with parameters ( $\beta = 6, \theta = 1$ ). Third and fourth rows are the results for normal test images, IMD014 and ISIC\_0015130 using ISODATA and MOMENT techniques, respectively. The corresponding operating parameters are ( $\beta = 2, \theta = 1$ ) and ( $\beta = 4, \theta = 1$ ), respectively

**Table 1.** Performance of the proposed method using five threshold-based techniques and thirteen channels from four colour spaces. Letter F denotes Dice score less than 0.65. Red-coloured numbers are Dice scores recorded after the application of threshold correction factor.

Threshold Methods	Colour Space Channel												
	r	g	b	G	h	s	v	L	A	B	x	y	z
ISODATA ([27])	F	0.66(0.31)	F	F	F	0.83(0.2)	F	F	F	F	F	F	0.68(0.39)
MEAN ([28])	F	F	F	F	F	0.82(0.26), <b>0.91(0.20)</b>	F	F	0.66(0.32)	0.72(0.32)	F	F	F
MINERROR ([26])	F	F	0.74(0.32)	F	F	0.82(0.24), <b>0.85(0.18)</b>	F	F	F	0.69(0.33)	F	F	0.70(0.30)
MOMENT ([29])	F	F	0.68(0.39)	F	F	0.81(0.12)	F	F	F	F	F	F	0.65(0.40)
OTSU ([30])	F	0.67(0.31)	F	0.65(0.31)	F	0.83(0.15)	F	F	F	F	F	F	0.71(0.36)

**Table 2.** Correlation coefficient between performance of proposed method (implemented in the saturation channel with five binarization techniques) and five dataset attributes.

Dataset Attributes	Threshold Methods				
	ISODATA [27]	MEAN [28]	MINERROR [26]	MOMENT [29]	OTSU [30]
<b>D1</b>	0.24	0.01	-0.02	0.20	0.26
<b>D2</b>	0.07	0.34	0.10	-0.21	0.02
<b>D3</b>	-0.12	-0.18	-0.10	-0.07	-0.14
<b>D4</b>	0.01	0.03	-0.04	0.01	-0.04
<b>D5</b>	0.05	-0.17	-0.29	0.10	0.10

### 3.2 Analysis of Results and Correction Factor

The relationship between the Dice score-based performance of the proposed method and the five attributes of the datasets was quantified using the Spearman rank correlation coefficient  $\rho$  [31]:

$$\rho = 1 - \frac{6 \sum_{i=1}^L t_i^2}{L(L^2 - 1)} \quad (11)$$

where  $t_i$  is the difference between the two ranks of each observation and  $L = 600$  is the number of observations. The correlation coefficients displayed in Table 2 suggest the followings (1) the MEAN and MINERROR binarization techniques are more robust to variations in perceptual quality. (2) Lesion size can influence the MEAN and MOMENT binarization techniques. (3) Lesion position and eccentricity does not significantly influence segmentation accuracy. (4) The level of cluttering and occluding objects have significant influence on the performance of the proposed method implemented with MEAN and MINERROR techniques. Based on this analysis, we conclude that correction factor can enhance the performance of the MEAN and MINERROR techniques. The MEAN technique tend to underestimate the threshold in the presence of cluttering and occluding objects leading to oversegmentation. We consider that, cluttering and occluding

objects, in the absence of other confounding factors, contribute to the relative contrast as well as the ratio of class sizes in the image. To compensate for this shortcomings we determine, for each image, a correction factor  $\alpha$  defined as

$$\alpha = 1 + \left( \frac{1}{sE} \right) \quad (12)$$

The reasoning behind the correction factor is that images with increasing spatial extent tend to be homogeneous, so the corrected threshold  $\mu_c \approx \mu$ . Conversely, images with lower spatial extent tends to be heterogeneous, so the corrected threshold  $\mu_c > \mu$ . The correction factor is multiplied with the average pixel intensity level of the test image.

The MINEROR technique is robust to the size of lesion but in the presence of occluding objects, it overestimate the threshold leading to undersegmentation. To address this problem, we adopt the mean value of pixels  $\mu$  as the reference threshold. Then we define a new threshold  $T$ :

$$T = \begin{cases} T_1 & \text{if } \left( \frac{T_1}{\mu} \right) \leq 1.5 \\ T_2 & \text{if Otherwise} \end{cases} \quad (13)$$

where  $T_1$  is the MINEROR threshold, and  $T_2$  are the threshold levels computed using any of ISODATA, MOMENT and OTSU techniques. The reasoning here is to leverage the robustness of ISODATA, MOMENT and OTSU techniques to the level of occluding objects.

### 3.3 Evaluation with Correction Factor

Correction factor was applied to the MEAN and MINEROR techniques according to Eq. 12 and Eq. 13. Then we repeat the evaluation of the proposed method for the saturation channel of the HSV colour space. The segmentation accuracy (red colour in Table 1) improved from 0.82 to 0.91 for the MEAN technique and from 0.82 to 0.85 for the MINEROR technique.

## 4 Conclusions and Future Work

Although image segmentation of skin lesions has been successfully addressed in many studies, there is need to improve the performance of several techniques. Challenges encountered in skin lesion segmentation include confounding factors such as skin hairs. Some pre-processing steps designed to address these challenges reduce the efficacy of a CAD system. We hereby propose a new method to segment skin lesion in dermatoscopy images without the need for hair removal preprocessing step. Binarization technique incorporated into the preliminary segmentation stage makes it potentially efficient and the proposed method is robust to images with different attributes. Parameters which define the algorithm operation can be either manually or automatically adjusted to optimize segmentation accuracy. Furthermore, the different steps in the implementation of

the algorithm are linked by parameters which encourages automation, an important attribute for effective computer-aided diagnosis. Future research direction will focus on utilizing a much larger volume of dataset. We will explore other approaches to compute the correction factor for the different binarization techniques. The influence of the algorithm parameters on segmentation accuracy will be investigated.

## References

1. M EMRE Celebi, QUAN Wen, HITOSHI Iyatomi, KOUHEI Shimizu, H Zhou, and G Schaefer. A state-of-the-art survey on lesion border detection in dermoscopy images. *Dermoscopy Image Analysis*, pages 97–129, 2015.
2. Cila Herman. Emerging technologies for the detection of melanoma: achieving better outcomes. *Clinical, cosmetic and investigational dermatology*, 5:195, 2012.
3. Harold Kittler, H Pehamberger, K Wolff, and M Binder. Diagnostic accuracy of dermoscopy. *The lancet oncology*, 3(3):159–165, 2002.
4. Cristiane Benvenuto-Andrade, Stephen W Dusza, Jennifer L Hay, Anna Liza C Agero, Allan C Halpern, Alfred W Kopf, and Ashfaq A Marghoob. Level of confidence in diagnosis: clinical examination versus dermoscopy examination. *Dermatologic surgery*, 32(5):738–744, 2006.
5. Ilias Maglogiannis and Charalampos N Doukas. Overview of advanced computer vision systems for skin lesions characterization. *IEEE transactions on information technology in biomedicine*, 13(5):721–733, 2009.
6. Omar Abuzaghlleh, Buket D Barkana, and Miad Faezipour. Noninvasive real-time automated skin lesion analysis system for melanoma early detection and prevention. *IEEE journal of translational engineering in health and medicine*, 3:1–12, 2015.
7. Roberta B Oliveira, E Mercedes Filho, Zhen Ma, João P Papa, Aledir S Pereira, and João Manuel RS Tavares. Computational methods for the image segmentation of pigmented skin lesions: a review. *Computer methods and programs in biomedicine*, 131:127–141, 2016.
8. Lequan Yu, Hao Chen, Qi Dou, Jing Qin, and Pheng-Ann Heng. Automated melanoma recognition in dermoscopy images via very deep residual networks. *IEEE transactions on medical imaging*, 36(4):994–1004, 2017.
9. Tim Lee, Vincent Ng, Richard Gallagher, Andrew Coldman, and David McLean. Dullrazor®: A software approach to hair removal from images. *Computers in biology and medicine*, 27(6):533–543, 1997.
10. Kimia Kiani and Ahmad R Sharafat. E-shaver: An improved dullrazor® for digitally removing dark and light-colored hairs in dermoscopic images. *Computers in biology and medicine*, 41(3):139–145, 2011.
11. Feng-Ying Xie, Shi-Yin Qin, Zhi-Guo Jiang, and Ru-Song Meng. Pde-based unsupervised repair of hair-occluded information in dermoscopy images of melanoma. *Computerized Medical Imaging and Graphics*, 33(4):275–282, 2009.
12. Qaisar Abbas, Irene Fondón Garcia, M Emre Celebi, and Waqar Ahmad. A feature-preserving hair removal algorithm for dermoscopy images. *Skin Research and Technology*, 19(1):e27–e36, 2013.
13. Maciel Zortea, Eliezer Flores, and Jacob Scharcanski. A simple weighted thresholding method for the segmentation of pigmented skin lesions in macroscopic images. *Pattern Recognition*, 64:92–104, 2017.

14. Mario Rosario Guarracino and Lucia Maddalena. Sdi+: A novel algorithm for segmenting dermoscopic images. *IEEE journal of biomedical and health informatics*, 23(2):481–488, 2019.
15. Alexander Wong, Jacob Scharcanski, and Paul Fieguth. Automatic skin lesion segmentation via iterative stochastic region merging. *IEEE Transactions on Information Technology in Biomedicine*, 15(6):929–936, 2011.
16. Y. Yuan, M. Chao, and Y. Lo. Automatic skin lesion segmentation using deep fully convolutional networks with jaccard distance. *IEEE Transactions on Medical Imaging*, 36(9):1876–1886, Sep. 2017.
17. L. Bi, J. Kim, E. Ahn, A. Kumar, M. Fulham, and D. Feng. Dermoscopic image segmentation via multistage fully convolutional networks. *IEEE Transactions on Biomedical Engineering*, 64(9):2065–2074, Sep. 2017.
18. Nabin K Mishra and M Emre Celebi. An overview of melanoma detection in dermoscopy images using image processing and machine learning. *arXiv preprint arXiv:1601.07843*, 2016, 2016.
19. T Hoang Ngan Le and Marios Savvides. A novel shape constrained feature-based active contour model for lips/mouth segmentation in the wild. *Pattern Recognition*, 54:23–33, 2016.
20. Tomas Majtner, Kristina Lidayova, Sule Yildirim-Yayilgan, and Jon Yngve Hardeberg. Improving skin lesion segmentation in dermoscopic images by thin artefacts removal methods. In *Visual Information Processing (EUVIP), 2016 6th European Workshop on*, pages 1–6. IEEE, 2016.
21. Devansh Bisla, Anna Choromanska, Russell S. Berman, Jennifer A. Stein, and David Polsky. Towards automated melanoma detection with deep learning: Data purification and augmentation. In *The IEEE Conference on Computer Vision and Pattern Recognition (CVPR) Workshops*, June 2019.
22. Qaisar Abbas, M Emre Celebi, and Irene Fondón García. Hair removal methods: a comparative study for dermoscopy images. *Biomedical Signal Processing and Control*, 6(4):395–404, 2011.
23. M. Osadebey, M. Pedersen, and D. Waaler. Plant leaves region segmentation in cluttered and occluded images using perceptual color space and k-means-derived threshold with set theory. In *2019 IEEE 17th International Conference on Industrial Informatics (INDIN)*, volume 1, pages 1211–1216, July 2019.
24. Neeraj Kumar, Alexander Berg, Peter N Belhumeur, and Shree Nayar. Describable visual attributes for face verification and image search. *IEEE Transactions on Pattern Analysis and Machine Intelligence*, 33(10):1962–1977, 2011.
25. Anish Mittal, Anush Krishna Moorthy, and Alan Conrad Bovik. No-reference image quality assessment in the spatial domain. *IEEE Transactions on Image Processing*, 21(12):4695–4708, 2012.
26. Josef Kittler and John Illingworth. Minimum error thresholding. *Pattern recognition*, 19(1):41–47, 1986.
27. TW Ridler, S Calvard, et al. Picture thresholding using an iterative selection method. *IEEE trans syst Man Cybern*, 8(8):630–632, 1978.
28. Chris A Glasbey. An analysis of histogram-based thresholding algorithms. *CVGIP: Graphical models and image processing*, 55(6):532–537, 1993.
29. Wen-Hsiang Tsai. Moment-preserving thresholding: A new approach. *Computer Vision, Graphics, and Image Processing*, 29(3):377–393, 1985.
30. Nobuyuki Otsu. A threshold selection method from gray-level histograms. *IEEE transactions on systems, man, and cybernetics*, 9(1):62–66, 1979.
31. Edgar C Fieller, Herman O Hartley, and Egon S Pearson. Tests for rank correlation coefficients. i. *Biometrika*, 44(3/4):470–481, 1957.